Mechanistic Insights into Polymerization-Induced Self-Assembly Using Maleimide-Based Fluorophores

Pearce, Amanda K.; Parkinson, Sam J.; Akar, Irem; Derry, Matthew J.; Topham, Paul D.; Mathers, Robert T.; Stavros, Vasilios G.; O'reilly, Rachel k.

DOI:
10.1021/acs.macromol.3c01451

Document Version
Publisher's PDF, also known as Version of record

Citation for published version (Harvard):
Pearce, AK, Parkinson, SJ, Akar, I, Derry, MJ, Topham, PD, Mathers, RT, Stavros, VG & O'reilly, RK 2023, 'Mechanistic Insights into Polymerization-Induced Self-Assembly Using Maleimide-Based Fluorophores', *Macromolecules*, vol. 56, no. 23, pp. 9443-9454. https://doi.org/10.1021/acs.macromol.3c01451

Macromolecules

Open Access

pubs.acs.org/Macromolecules

Article

Mechanistic Insights into Polymerization-Induced Self-Assembly Using Maleimide-Based Fluorophores

Amanda K. Pearce, Sam J. Parkinson, Irem Akar, Matthew J. Derry, Paul D. Topham, Robert T. Mathers, Vasilios G. Stavros, and Rachel K. O'Reilly*

Cite This: *Macromolecules* 2023, 56, 9443–9454

Read Online

ACCESS | Metrics & More | Article Recommendations | Supporting Information

ABSTRACT: Polymerization-induced self-assembly (PISA) is a versatile and readily accessible method to produce nanoparticles of various morphologies in situ as polymerization progresses. PISA exploits the chain extension of a solvophilic macromolecular chain-transfer agent with monomers that are miscible in the continuous phase but form a solvophobic, immiscible polymer, driving self-assembly. However, the ability to monitor in situ the onset of self-assembly and the evolution of morphology during the PISA process remains a significant challenge, which critically limits our understanding of the mechanisms of particle formation. In this work, we demonstrate that a maleimide-based small-molecule fluorophore can act as a powerful probe to study PISA over time using fluorescence and fluorescence lifetime as outputs. We show that the aminochloromaleimide (ACM) fluorophore can be readily incorporated within a PISA system to produce fluorescent nanostructures without affecting their final morphology in comparison to their nonfluorescent analogues. The ACM probe exhibits diagnostic increases in fluorescence lifetime first with the onset of self-assembly and then with the evolution of particle morphology in the order of spheres > vesicles > worms. Excitingly, monitoring the change in fluorescence lifetime in situ during PISA yielded insights into the mechanism of particle formation when targeting higher-order morphologies. Finally, we demonstrate that these maleimide-functionalized nanostructures can be used as cell imaging agents using fluorescence lifetime imaging microscopy (FLIM), whereby each morphology produces distinct lifetime decay patterns within a cell environment. Overall, we envision this becoming a powerful tool for the analysis of nanoparticle states within complex environments, inspiring further investigations of the study of PISA using this simple and accessible method.

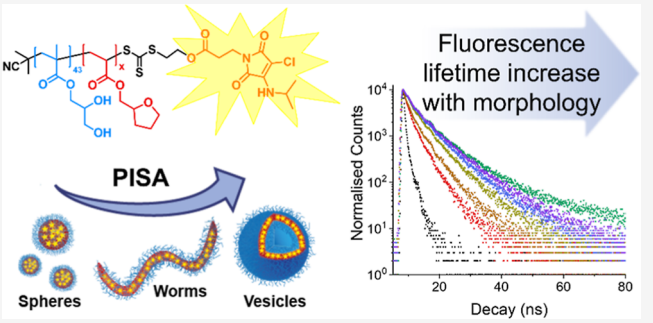

INTRODUCTION

The field of block copolymer self-assembly has received significant academic and industrial interest over the past few decades owing to its exciting applications spanning chemistry, biology, materials, and physics.[1] Inspired by the plethora of intricate assemblies found in nature, researchers have been inspired to understand the mechanisms behind molecular self-assembly in order to produce, with precision, increasingly sophisticated nanoscale structures.[2] Recent synthetic advances in controlled radical polymerizations have enabled the targeted formation of artificial polymeric materials with higher-order structures, evolving from simple spherical micelles into more complex one- and two-dimensional worms, vesicles, and platelets.[2−4] However, this evolving complexity is accompanied by significant challenges in characterizing the self-assembly pathways, limiting our overall understanding of ways of targeting specific nanoparticle morphologies through a rational experimental design. The ability to understand how changes in polymer design and assembly conditions impact the final nanoscale morphology by studying the self-assembly process in situ would provide critical insights toward achieving materials with tailored structures and functionalities.

We are especially interested in the study of polymerization-induced self-assembly (PISA). This versatile and readily accessible method enables the production of nanoparticles of various morphologies in situ as the polymerization progresses.[5] PISA involves chain-extension of a solvophilic macromolecular chain-transfer agent with monomers that are miscible with the continuous phase but form a solvophobic, immiscible polymer, which drives self-assembly. Amenable to a wide variety of reaction conditions and monomer chemistries, PISA has become an invaluable method for nanoparticle production across many research fields.[6,7] However, challenges in studying the onset of self-assembly and the evolution of morphology in

Received: July 21, 2023
Revised: October 12, 2023
Accepted: November 10, 2023
Published: November 30, 2023

Scheme 1. (A) Reaction Schematic for the Synthesis of Maleimide-Functionalized Block Copolymers and (B) Cartoon Depicting the Self-Assembled Polymer Systems Targeted in This Work, Showing Spheres, Worms, and Vesicles with Maleimide Units Localized within the Hydrophobic Core

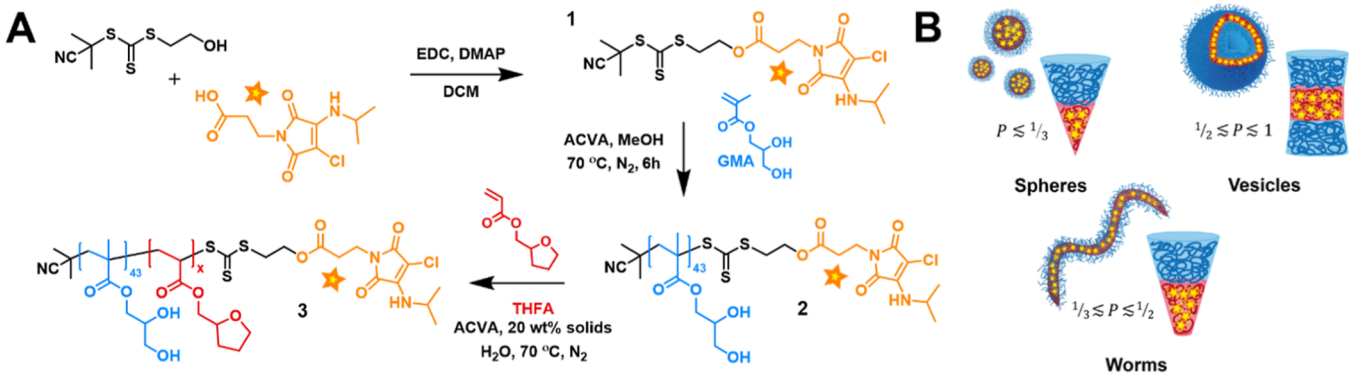

situ during PISA have critically limited our mechanistic understanding of the process to date. In particular, the final nanostructures produced during PISA can often be dynamic and kinetically trapped, and their assembly process involves passing through a range of initial transition states and spontaneous organization steps resulting from different intermolecular forces to achieve their final morphology.[8,9] We note that in situ small-angle X-ray scattering (SAXS) has been demonstrated to sensitively monitor the morphological transitions during PISA;[10,11] however, this requires highly specialized equipment and expertise, which limits the practicality of this method. Overall, a complete understanding of the PISA process requires a readily accessible characterization methodology with high sensitivity, a fast response time, and the ability to be performed with particles in their native hydrated state. In this work, we aim to address this important research challenge.

Small-molecule fluorescent probes, which change their fluorescence properties in response to a binding event, chemical reaction, or change in the immediate environment, are among the most utilized spectroscopy tools.[12,13] Such probes have historically found use in drug discovery,[14] sensing,[13,15−17] environmental analysis,[18,19] and cellular imaging.[20−23] More recently, fluorophores have also been employed in the study of macromolecular self-assembly events, for example, to probe the structures of porphyrins,[24,25] aggregation/assembly of peptides,[26,27] formation of hydrogel networks,[28,29] and more.[30,31] These advances have been made possible by the high sensitivity and great accessibility of fluorescence as a spectroscopic technique, in addition to the wide array of available fluorophores.[32−34] Small-molecule probes can be chemically modified to tune spectroscopic properties, and their small size enables incorporation into systems without compromising the overall structure or function, enabling the investigation of the true environment. Maleimide-based fluorophores are particularly interesting probes for application as biological and chemical sensors due to their facile structural modification, high emissivity, and sensitivity.[35−43]

Focusing on fluorophores as reporters of polymer self-assembly, we have shown previously that the inclusion of a maleimide unit within an amphiphilic block copolymer enabled the formation of self-reporting polymer micelles.[44] Photophysical characterization showed that the maleimide moiety could act as a reporter for micellization, whereby emission lifetime, anisotropy decay, and time-domain fluorescence lifetime imaging (FLIM) could rapidly resolve differences in the particle supramolecular state. Fluorescence lifetime is an intrinsic photophysical property that is independent of the local fluorophore concentration.[45,46] As such, it is an absolute measurement and relatively unaffected by artifacts due to scattered light and photobleaching, making its fluorescence lifetime measurements particularly powerful in the study of self-assembled structures.

More recently, Rho et al. included a pyrene unit within a PISA system with the aim of monitoring assembly in situ, where they were able to demonstrate differences in fluorescence emission as assembly occurred on account of the changing fluorophore environment.[47] However, only a fraction of polymer chain ends could be labeled with the pyrene unit using their synthetic strategy, and only fluorophore emission was studied, limiting mechanistic insights to the simple onset of assembly and final morphology.

Here, we rapidly accelerate progress in our understanding of the PISA process by using a maleimide-based fluorophore as an environmental probe. We hypothesized that in situ fluorescence lifetime measurements would provide quantitative evidence of the onset of particle formation, evolution of morphology, and, uniquely, any transition states during the assembly process in unprecedented detail. Furthermore, we expected that varied particle morphologies (spheres, worms, and vesicles) would provide distinctive lifetime decay curves on account of their different core environments. Finally, we set out to demonstrate the applicability of this technique for cell imaging using FLIM, with the anticipation that different particle morphologies and degradation behaviors could be readily deconvoluted when structures are imaged with the same fluorophore.

Synthesis and Characterization. Our essential design considerations were as follows: (1) a synthetic strategy whereby every polymer chain end could be reliably labeled with a maleimide unit without impacting the self-assembly process; (2) a polymer system amenable to particle formation in a pure aqueous environment to enable transfer into biological applications; and (3) a chemically tunable system to ensure wide applicability for future research endeavors. To achieve this, we synthesized a chain-transfer agent (CTA) for reversible addition−fragmentation chain transfer (RAFT) polymerization with a maleimide moiety coupled to the Z group (Scheme 1). An aminochloromaleimide (ACM)

https://doi.org/10.1021/acs.macromol.3c01451
Macromolecules 2023, 56, 9443−9454

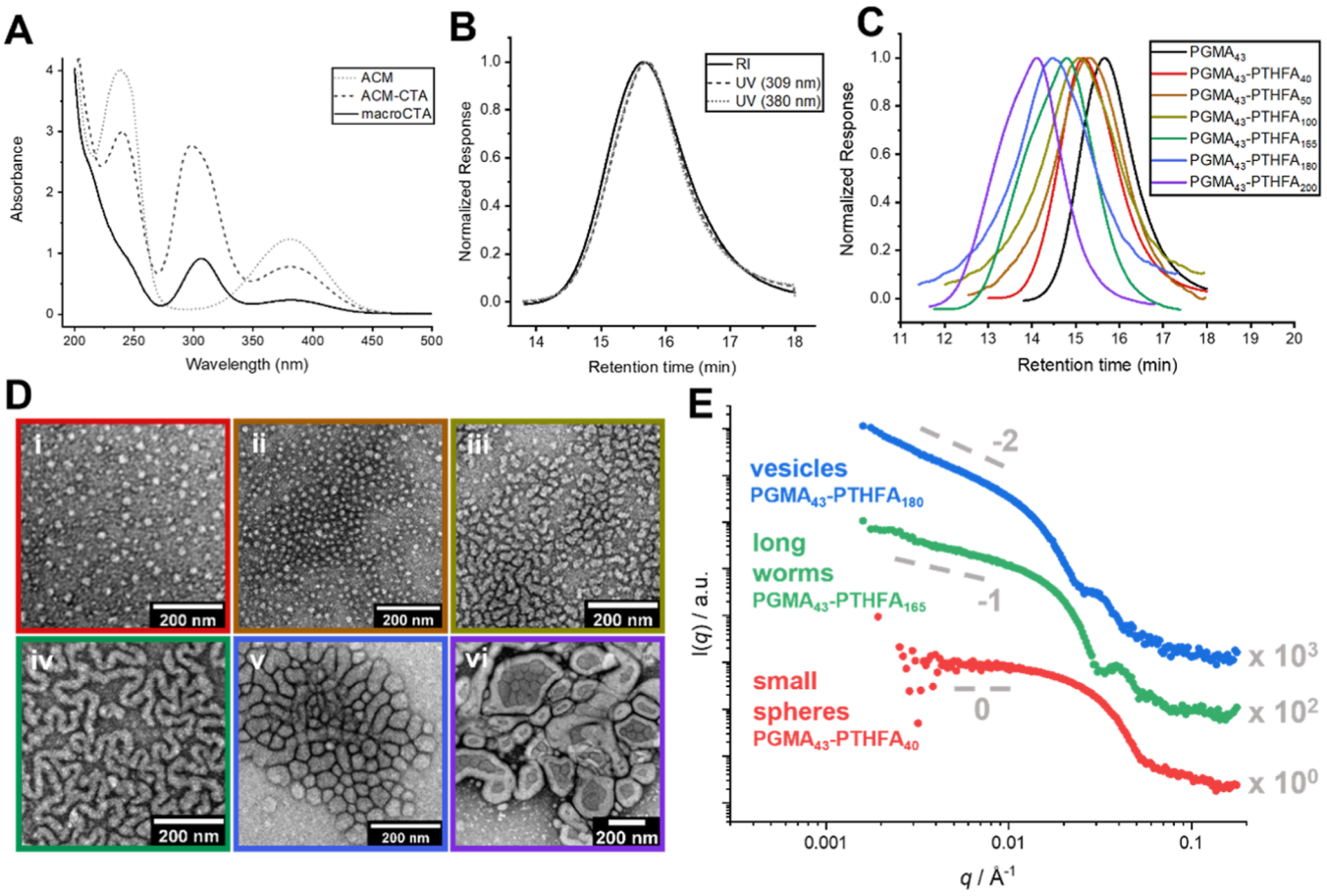

Figure 1. (A) UV−vis spectra confirming the presence of trithiocarbonate and maleimide absorbance peaks, (B) SEC trace of the macroCTA showing RI and UV detection at 309 and 380 nm, (C) SEC traces from the RI detections of PISA polymers, (D) dry-state TEM images of PISA morphologies confirming (i) small spheres, (ii) large spheres, (iii) short worms, (iv) long worms, (v) vesicles, and (vi) large vesicles, and (E) background-subtracted small-angle X-ray scattering profiles of small spheres, long worms, and vesicles confirming observed morphologies from dry-state TEM (N.B. the two upper patterns are offset by arbitrary factors for visual clarity and dashed lines indicate low q gradients of 0, −1, and −2 as a guide to the eye, indicating the presence of spheres, worms, and vesicles, respectively).

Table 1. Characterization Data for the Fluorescent $PGMA_{43}$ macroCTA and $PGMA_{43}$-$PTHFA_x$ Diblock Copolymers

GMA DP	THFA DP	Rxn wt %	M_n, NMR (kDa)	M_n, SEC[a] (kDa)	$Đ_M$[b]	D_h (nm)[c]	PDI	morphology[d]
43			6.8	6.6	1.1			
43	40	20	13.1	13.7	1.5	30	0.13	spheres
43	50	20	14.6	16.8	1.5	50	0.15	spheres
43	100	20	22.4	26.4	1.9	126	0.34	short worms
43	165	20	32.5	27.1	1.7	86	0.41	long worms
43	180	20	34.9	28.6	1.9	435	0.55	vesicles
43	200	20	38.0	36.7	1.7	412	0.43	large vesicles

[a]Determined by SEC analysis in DMF containing 5 mM NH_4BF_4. [b]$Đ_M = M_w/M_n$. [c]Determined by DLS at 0.01 wt % in Milli-Q H_2O. [d]Determined by TEM analysis.

derivative was chosen for this work as, thus far, this class is the brightest known of the maleimide dyes[35] and is widely reported and understood.[36] We chose glycerol monomethacrylate (GMA)[48] and tetrahydrofurfuryl acrylate (THFA) as the corona and core monomers, respectively, in order to achieve sterically stable particles in an aqueous environment with a sufficiently hydrophobic core (monomer log P_{oct} 1.31)[49] to assess subtle changes in the probe environment.

Polymerization of GMA yielded a water-soluble macroCTA with maleimide chain ends (see Scheme 1, Figure 1A, and Supporting Information for details). In this way, the probe would be situated within the growing hydrophobic polymer block, allowing for accurate environmental reporting during the polymerization. The polymerization was performed in methanol at 65 °C using 4,4′-azobis(4-cyanovaleric acid) (ACVA) as a thermal radical initiator and quenched at 90% conversion, achieving a final average degree of polymerization (DP) of 43. Size exclusion chromatography (SEC) analysis confirmed that the GMA macroCTA had a number-average molar mass (M_n) of 6.6 kDa and a dispersity ($Đ_M$) of 1.1. Importantly, the SEC trace showed good overlap of the refractive index (RI) and UV detectors at 309 nm (trithiocarbonate group) and 380 nm (maleimide group), highlighting the excellent end group fidelity on the macroCTA

https://doi.org/10.1021/acs.macromol.3c01451
Macromolecules 2023, 56, 9443−9454

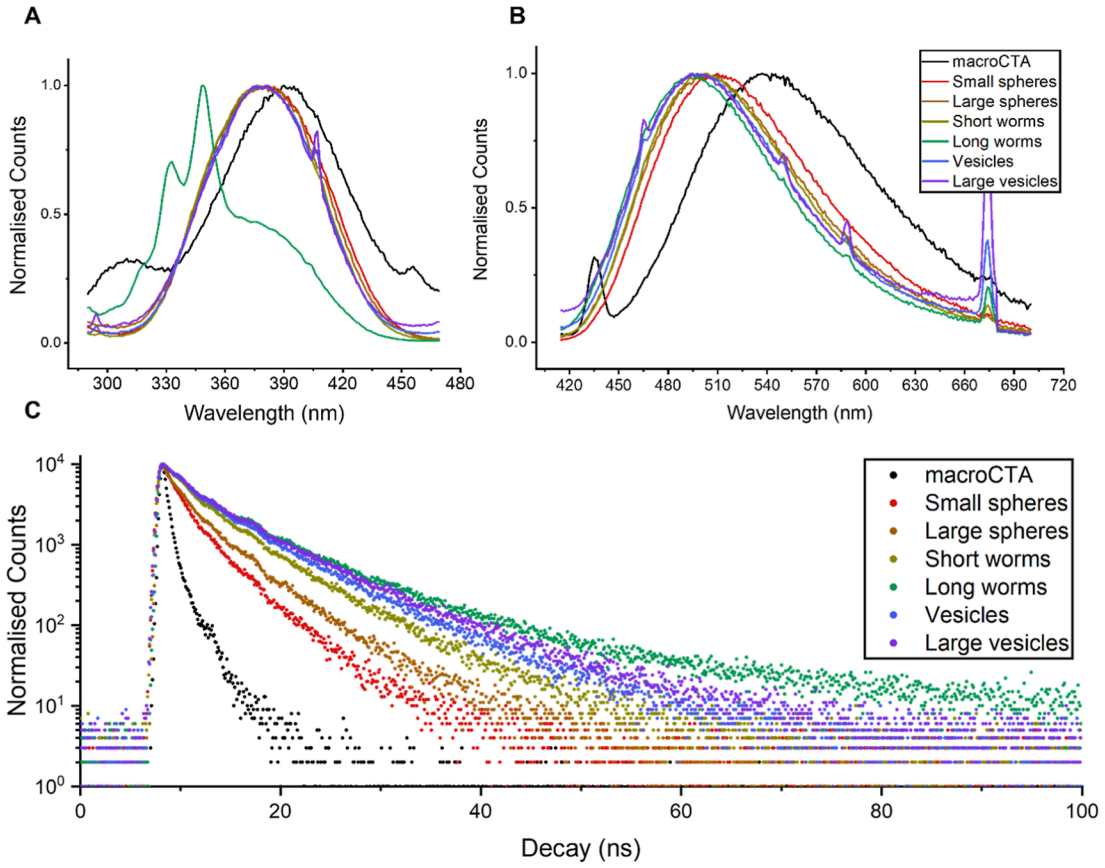

Figure 2. (A) Steady-state excitation, (B) emission spectra, and (C) fluorescence decay curves for the macroCTA and PISA morphologies in water.

Table 2. Photophysical Decay and Exponential Fitting on the Nanoparticles and Steady-State Emission Maxima

	τ_1 (ns)	Rel. %	τ_2 (ns)	Rel. %	τ_3 (ns)	Rel. %	lifetime (ns)	emission (nm)
macroCTA	0.3	56.3	0.9	38.9	3.1	4.9	0.8	535
small spheres	1.2	45.6	3.6	50.1	7.5	4.3	3.6	510
large spheres	1.1	21.1	3.3	54.1	6.6	24.9	4.7	505
short worms	2.1	27.4	5.1	55.9	8.8	16.7	5.9	502
long worms	2.1	20.1	7.1	70.1	24.2	9.8	12	494
vesicles	1.7	18.2	5.4	59.4	9.9	22.4	7.0	498
large vesicles	2.1	18.8	5.6	51.8	10.5	29.5	7.8	498

(Figure 1A,B). Subsequently, a series of PISA experiments were performed targeting a range of core DP values from 40 to 200 at 20 wt % solids in order to access a variety of nanoparticle morphologies. Each PISA reaction reached full monomer conversion within 8 h, as confirmed by ^{1}H NMR spectroscopic kinetic analysis. The final polymers were analyzed by SEC, which confirmed the quantitative blocking efficiency as well as the full retention of the macroCTA and maleimide UV signals on the polymer chains (Figure 1C). We were able to observe a range of morphologies ranging from spheres (DP = 40), large spheres (DP = 50), short worms (DP = 100), long worms (DP = 165), vesicles (DP = 180), and large vesicles (DP = 200), as confirmed by dry-state TEM analysis (Figure 1D, Table 1). These morphologies were further corroborated by collecting the small-angle X-ray scattering (SAXS) patterns of small spheres, long worms, and vesicles (Figure 1E) using a synchrotron SAXS beamline.[50] The radially integrated patterns obtained for these $PGMA_{43}$-$PTHFA_y$ particles were plotted as X-ray scattering intensity, $I(q)$, vs the scattering vector, q, and demonstrated the expected gradients at low q of approximately zero for spheres, −1 for worms, and −2 for vesicles.[51] Together, these data unequivocally confirm that the full range of nanoparticle morphologies was achieved.

Pleasingly, the full range of higher-order morphologies could be obtained when solely using the maleimide-functionalized macroCTA, indicating that the presence of the small probe on the chain ends did not impact assembly. This was confirmed by targeting the same polymer DPs using a nonfluorescent control macroCTA, which showed similar morphologies at the same DP values (Figures S17−S19, Table S1).

Steady-State Fluorescence and Fluorescence Lifetime Decay. We next sought to establish how the nanoparticle morphology influenced the fluorescent properties of the maleimide fluorophore. Steady-state excitation and emission spectra of the macroCTA in an aqueous solution showed an excitation maximum (λ_{Ex}) of 385 nm and emission maximum (λ_{Em}) of 535 nm. Upon assembly into nanoparticle morphologies, all samples showed a slight shift in the excitation maxima (λ_{Ex} = 380 nm), with obvious blue-shifted emission

https://doi.org/10.1021/acs.macromol.3c01451
Macromolecules 2023, 56, 9443−9454

behavior to different extents depending on morphology (Figure 2A). Previous research into these probes has shown this same trend when moving from polar to nonpolar solvents, resulting from reduced dipole−dipole interactions and shielding the maleimide from electron-driven proton transfer quenching mechanisms.[52] In this system, the fluorophore in the macroCTA was initially exposed to the quenching aqueous environment; however, upon self-assembly, it became progressively more shielded by the inclusion of the hydrophobic monomer units. The nanoparticle emission maxima values spanned from 510 nm for the small spheres down to 494 nm for the long worms, showing a trend of subtle changes in optical properties with the evolution of morphology.

Solution-state time-correlated single-photon counting (TCSPC) was performed next to determine the emission decay profiles. Each nanoparticle solution and the macroCTA as control were assessed with a pulsed 405 nm diode laser (135 ps (full-width at half-maximum (fwhm)), and the resultant emission decays are presented in Figure 2B with exponential fitting details in Table 2. Every sample consistently displayed three components to decay after deconvolution, which were used to calculate average lifetime ($\tau_{av,A}$) values for an initial comparison. These results presented a more remarkable trend, whereby obvious increases in lifetime were observed in comparison to that of the macroCTA (0.8 ns). Polymerization to a core DP of 40 yielded small spheres with a lifetime of 3.6 ns, whereas targeting a core DP of 50 gave slightly larger spheres with an increased $\tau_{av,A}$ value of 4.7 ns. When targeting a core DP of 100, short worms were produced with a $\tau_{av,A}$ of 5.9 ns, whereas vesicles (DP = 180) and large vesicles (DP = 200) further extended the lifetime out to 7.0 and 7.8 ns, respectively. Intriguingly, the biggest increase in lifetime was observed for the long worm sample (DP = 165), with a value of 12 ns. It is noteworthy that this morphology also showed a different trend in the excitation spectra, whereby sharp features can be observed in addition to the broad peak exhibited by all samples. In combination, these results indicate that the long worms facilitate a maleimide environment where different electronic (and possibly vibronic) transitions from the ground state to the excited states are favored. The prolonged lifetime displayed may be the result of intersystem crossing to the lowest excited triplet state; however, further experimentation is required to confirm this observation.

In order to rule out the possibility that changes in lifetime decay were simply due to an increased hydrophobic environment with increasing core DP, a control experiment was performed using a shorter macroCTA and varying the core DP over a limited range at the border between sphere and vesicle phases (GMA_{33}-$THFA_{40}$, spheres; GMA_{33}-$THFA_{50}$, spheres; GMA_{33}-$THFA_{60}$, spheres/vesicles) at 10 wt % to minimize phase transitions (Table S2). Pure sphere morphologies yielded steady-state emission maxima of 504 nm and average lifetime decay values of 4.8 ns, whereas the mixed sphere/vesicle morphology showed a minute blue-shift in the emission maximum to 502 nm and a more dramatic shift of lifetime decay to 6.1 ns (Figures S24 and S25, Table S2). This confirmed that increasing the core block DP alone did not sufficiently explain the increase in lifetime decay values and that nanoparticle morphology plays a defining role.

To probe this further, each lifetime decay curve was subsequently analyzed with an exponential reconvolution fit (Table 2). For the macroCTA, the maleimide decays almost immediately, with two subnanosecond lifetimes comprising much of the average decay and a third slightly longer decay of 3.1 ns. The shortest decays are attributed to nonemissive aggregation and solvent-collision effects, and the longest lifetime is the intrinsic relaxation event (excited-state lifetime of the isolated probe) for the maleimide fluorophore.[44]

Upon examining the deconvoluted lifetime decay profiles of the nanoparticles, it could be seen that regardless of morphology, each decay component was prolonged in comparison to the macroCTA. First, each τ_1 component, which we have attributed to the intrinsic lifetime of the maleimide in each particle, was increased above 1 ns and, except for the small spheres, comprised less than 30% of the total decay. This behavior confirms that upon self-assembly, the maleimide is more protected from the external aqueous environment, in agreement with the observations from the steady-state fluorescence data. Of particular interest is the analysis of the τ_2 and τ_3 components, which provide quantitative evidence that the environmental state of the maleimide changes with morphology. For example, increasing the number of spheres to the higher-order morphologies of worms and vesicles increased the value of τ_2 to above 5 ns, with this contributing more than 55% of the overall lifetime decay. Perhaps even more characteristic, when considering τ_3, it can be clearly seen that this value slowly increases as morphology evolves from spheres to worms to vesicles as well as its contribution to the overall decay profile.

Taken together, these data strongly suggest that the prolonged nanoparticle lifetimes compared to those of the macroCTA cannot be sufficiently explained by shielding from the aqueous environment alone. It is clear from the changes in fluorophore lifetime that the physical state of the fluorophore is changing within each morphology. However, understanding the mechanism for this is likely to be complex and beyond the scope of this study. We can hypothesize that there is a different packing of the maleimide moiety within the core of each morphology, enabled by the different core curvature as shown in Scheme 1B, as well as the restricted molecular movement that results from immobilization within the core environment.[43] It is also possible that the exclusion of water from the core region is varied for each morphology. Of great interest, the long worm morphology displays the longest τ_3 value, which supports our observations from the absorbance data that different electronic transitions are occurring toward longer lifetime states.

Overall, we attribute the longer τ_2 and τ_3 values to better and different fluorophore protection when in the self-assembled state and propose that each component extraction provides unique fingerprinting for characterization of morphology using fluorescence.

Monitoring of PISA Kinetics during Self-Assembly. Next, we validated the ability for the maleimide fluorophore to give a detailed analysis of the PISA process as polymerization of the core block occurred. For this validation, we chose to investigate the highest DP (200, large vesicles) to enable the study of each transitional morphology that occurred during the polymerization. As described above, two PISA experiments were performed side-by-side, each targeting a final core DP = 200. One experiment was left untouched, while the second was sampled every 10 min for the first hour and then every hour until quantitative conversion was reached. Kinetics were compared across both experiments to ensure that sampling did not impact the polymerization (Figure S26). Each sample was then diluted 100 times, analyzed for both steady-state

https://doi.org/10.1021/acs.macromol.3c01451
Macromolecules 2023, 56, 9443−9454

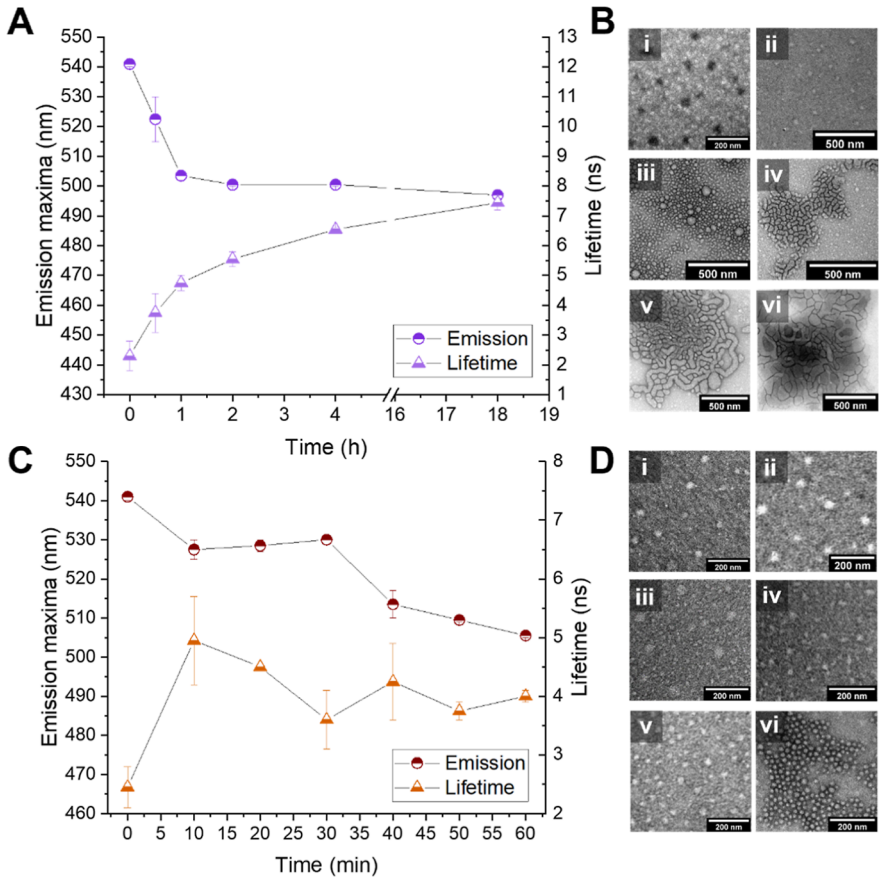

Figure 3. (A) Emission maxima and average fluorescent lifetimes of large vesicles with kinetic sampling, (B) dry-state TEM images confirming morphology at each time point for (i) 0, (ii) 0.5, (iii) 1, (iv) 2, (v) 4, and (vi) 18 h; (C) emission maxima and average fluorescent lifetimes of large vesicles with kinetic sampling within the first 60 min, (D) dry-state TEM images confirming morphology at each time point for (i) 10, (ii) 20, (iii) 30, (iv) 40, (v) 50, and (vi) 60 min.

Table 3. Photophysical Decay and Exponential Fitting on the Large Vesicles and Steady-State Emission Maxima

time	τ_1 (ns)	Rel. %	τ_2 (ns)	Rel. %	τ_3 (ns)	Rel. %	lifetime (ns)	emission (nm)
0 min	0.4	60.2	1.3	31.0	5.3	8.8	2.8	540
10 min	0.2	24.5	1.3	36.4	6.7	39.1	5.7	525
20 min	0.2	29.8	1.2	46.8	6.0	23.4	4.5	530
30 min	0.3	34.3	1.1	50.8	4.9	15.0	3.1	530
40 min	0.1	16.1	1.4	49.2	6.1	34.7	4.9	510
50 min	0.9	46.7	3.1	44.7	7.6	8.6	3.9	510
60 min	1.1	39.4	3.7	52.6	6.8	8.0	3.9	506
360 min	2.1	18.8	5.6	51.8	10.5	29.5	7.8	498

emission and lifetime decay behavior, and verified for the presence of self-assembly using dry-state TEM. It should be noted that due to the high weight percentages required for the PISA process, the polymerizations cannot be performed and analyzed within the fluorescence spectrometer as the high fluorophore content provides inaccurate results due to the oversaturation of the detector.

Fluorescence steady-state and lifetime measurements in conjunction with dry-state TEM imaging were able to monitor the evolution of the nanoparticle morphology as the polymerization progressed. Table S3 shows the blue-shifted emission maxima and the increase in average lifetime decay over time (Figure 3A, raw data shown in Figures S27−S29). Of interest is the time 0 value, which has a slightly longer $\tau_{av,A}$ of 2.8 ns in comparison to 0.8 ns for the macroCTA alone in solution. We attribute this to the presence of the core monomer in the starting formulation, providing small pockets of hydrophobic environment for maleimide shielding (discussed further below). We first analyzed the data after the onset of assembly at 60 min, where a clear spherical morphology can be seen in the TEM images (Figure 3B). Beyond this point, the in situ emission and lifetime behavior very closely match those of the individually isolated morphologies. Specifically, at 2 h, short worms have formed with an λ_{Em} of 500 nm and $\tau_{av,A}$ of 5.8 ns, compared to the short worms from above with an λ_{Em} of 502 nm and $\tau_{av,A}$ of 5.9 ns. The vesicle morphology was observed in situ after 4 h, with an λ_{Em} of 500 nm and $\tau_{av,A}$ of 6.7 ns compared to the above vesicles with an λ_{Em} of 498 nm and $\tau_{av,A}$ of 7.0 ns. Finally, the large vesicles were obtained after 18 h of reaction, with an λ_{Em} of 498 nm and $\tau_{av,A}$ of 7.4 ns in agreement with the above data. This confirms that the data for the known nanoparticle morphologies can be used to rapidly,

https://doi.org/10.1021/acs.macromol.3c01451
Macromolecules 2023, 56, 9443−9454

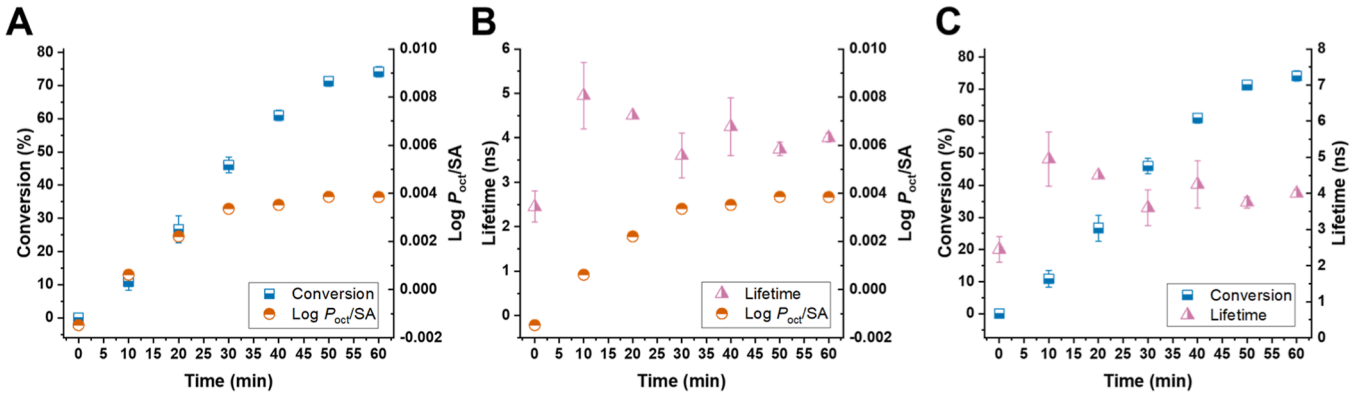

Figure 4. Plots demonstrating relationships between (A) THFA conversion and log P_{oct}/SA versus time, (B) fluorescence lifetime and log P_{oct}/SA versus time, and (C) THFA conversion and fluorescence lifetime versus time.

and with accuracy, identify morphological evolution simply by using fluorescence analysis.

Subsequently, we explored the data collected before the initial onset of assembly into spheres, with the hypothesis that this could provide insight into the mechanism of PISA in the early stages of polymerization. As above, we analyzed the collected data using fluorescence and TEM (raw data shown in Figures S30–S32), which revealed an unusual trend particularly in the average lifetime values (Figure 3C, Table 3). We observed a significant rapid increase in maleimide $\tau_{av,A}$ and blue-shifting of λ_{Em} within the first 10 min, from 2.8 to 5.7 ns and 540 to 525 nm, respectively. By 30 min, the lifetime had slightly decreased to 3.1 ns and the emission maximum had red-shifted to 530 nm. However, at 40 min, the lifetime once again increased to 4.9 ns and emission was blue-shifted to 510 nm. At 50 min, the emission maximum remained constant; however, the lifetime decreased back to 3.9 ns where it remained at 60 min, where the onset of initial assembly was complete.

Applying the deconvolution provided additional insight into this seemingly random trend of the initial 60 min. At time 0, the decays of <1.3 ns as identified for the macroCTA in solution can be observed. Until 30 min, these τ_1 and τ_2 values remain constant; however, their percentage contribution to the average lifetime changes. Specifically, the relative % of τ_1 decreases sharply and then slowly increases, while the relative % of τ_2 increases. During this time, both the values and relative % of τ_3 change, with an initial increase to 6.7 ns and 39%, respectively, followed by a decrease down to 4.9 ns and 15% by 30 min. This indicates that the maleimide is still primarily located within an aqueous environment as the <1.3 ns decay components are present; however, some form of longer-range aggregation, or premicellar assemblies, occurs. These appear to form at low conversion very rapidly as the macroCTA begins chain extending with the core monomer. We hypothesize that initially, the free THFA molecules in solution are associated with one another, stabilized by the growing macroCTA. This would cause the initial dramatic change in fluorophore photophysical properties. As the polymerization continues toward the formation of micelles, the aggregates will shrink in size and become more ordered, reflected in the decreasing trend in relative % for τ_1. Around 40 min, we can observe that the onset of the initial sphere morphology starts to occur. At this point, τ_1 becomes difficult to measure [0.1 ns, which is below the fwhm of the diodes (135 ps)], with a shift in relative % to the longer decay events. By 50 min, both τ_1 and τ_2 most closely resemble those of the small spheres and show a less obvious change in the data at 60 min. Studying the TEM images in parallel (Figure 3F), we were able to observe the presence of small low-density spherical features at all time points from 10 min, with obvious spheres present at 60 min. Taken together, these data suggest that while defined spheres do not appear on the TEM analysis until 60 min, the actual onset of assembly occurs somewhere between 40 and 50 min where the τ_1 value increases from 0.1 to 0.9 ns.

We next analyzed two additional PISA formulations targeting spheres (DP = 40) and short worms (DP = 100) to understand whether this was a universal observation. During the first 60 min, the PISA experiment targeting spheres did not show this premicellar aggregation behavior, with no changes in lifetime or emission maxima before 60 min (Figure S33). Conversely, when targeting short worms, premicellar aggregation was observed albeit to a lesser extent (Figure S34). This suggests that this process occurs only when targeting higher-order morphologies, likely due to the higher concentration of core monomers in the reaction mixture. To the best of our knowledge, this is the first example of in situ characterization data showing the mechanism of particle formation in the preassembly state. Full characterization of this process using in situ small-angle X-ray scattering is underway and will be the focus of detailed future work in this area.

Computational Analysis Using Log P_{oct}/SA. In eq 1, the octanol–water partition coefficients (log P_{oct}) quantify the partitioning of solute molecules between immiscible phases. Indeed, negative Log P values denote molecules, such as GMA, that prefer the aqueous phase. In contrast, positive values for THFA (log P_{oct} = 1.31), CTA (log P_{oct} = 3.56), and the maleimide fluorophore (log P_{oct} = 3.97) indicate partition into the organic phase.

$$\log\ P_{oct} = \log\left(\frac{[\text{solute}_{octanol}]}{[\text{solute}_{water}]}\right) \quad (1)$$

Normalizing a thermodynamic parameter (i.e., log P_{oct}) with a structural parameter (i.e., surface area, SA) facilitates comparison of architectural differences resulting from monomer size and functionality as well as oligomer length.[53,54] We have previously shown that computational log P_{oct}/SA values provide insights into polymer behavior in solution.[55−57] Here, we applied this analysis to help gain insight into the formation of vesicles during the first hour of polymerization.

https://doi.org/10.1021/acs.macromol.3c01451
Macromolecules 2023, 56, 9443−9454

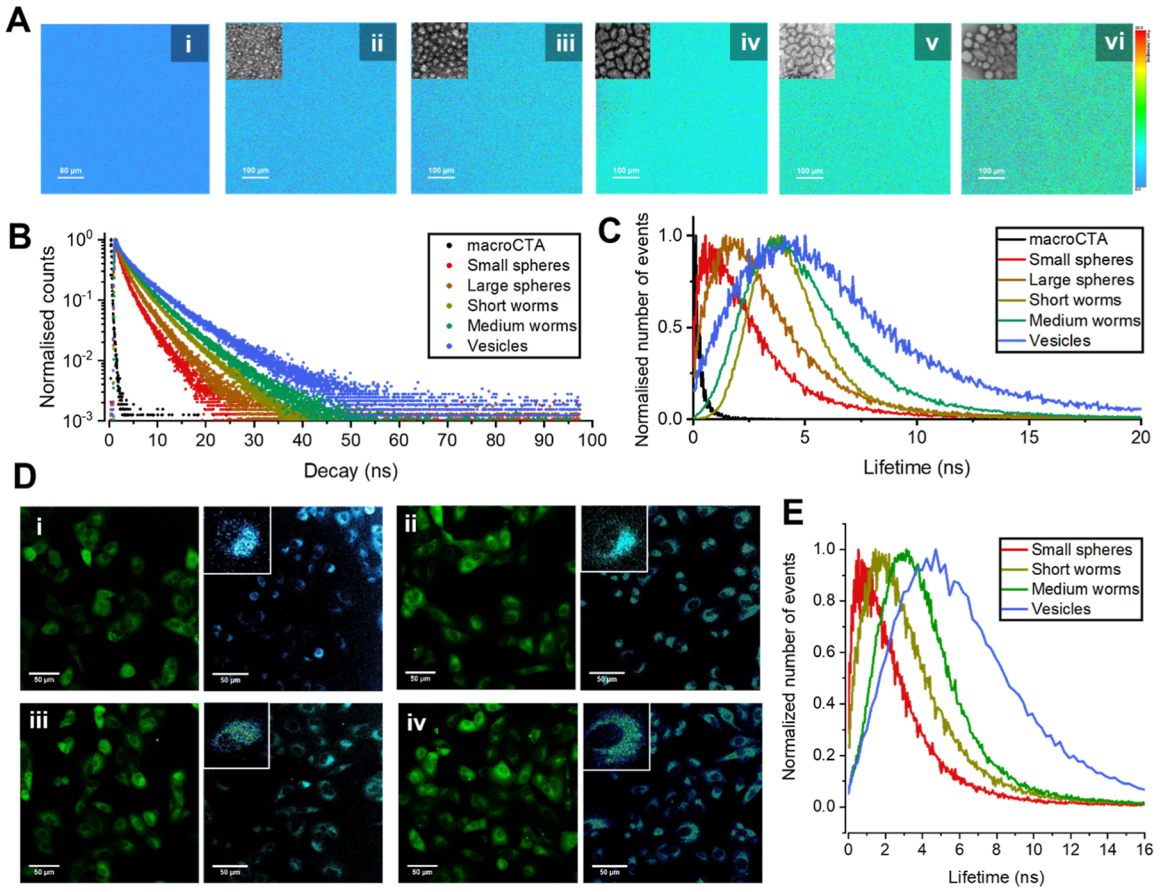

Figure 5. (A) FLIM images of (i) macroCTA, (ii) small spheres, (iii) large spheres, (iv) short worms, (v) medium worms, and (vi) vesicles as aqueous solutions on glass slides (inset from dry-state TEM images), (B) FLIM decay curves, and (C) fastFLIM histograms calculated from collected images shown in (A); (D) confocal and FLIM images of (i) spheres, (ii) short worms, (iii) medium worms, and (iv) vesicles, and (E) calculated fastFLIM histograms from the FLIM images shown in (D).

First, we constructed oligomeric molecular models with a ratio of GMA to THFA that matches the conversion of the growing copolymer (at T = 298 K). Then, log P_{oct} values were normalized by SA after molecular dynamics (MD) simulations (see Supporting Information for a detailed model). In Figure 4a, the conversion and log P_{oct}/SA were plotted against time. Before the polymerization of THFA, the macroCTA containing GMA units had a negative log P_{oct}/SA value. Interestingly, as the polymerization of THFA approached 11% conversion by the first 10 min time point, the negative log P_{oct}/SA value for the macroCTA became positive. As conversion continued, the hydrophobicity of the growing polymer chain increased before slowing down around 30 min.

Although a comparison of log P_{oct}/SA and lifetime values in Figure 4b did not reveal any obvious relationship, the largest changes in lifetime values occurred when values for log P_{oct}/SA were positive. Since the maleimide probe also has a positive log P_{oct}/SA value, we hypothesize that the fluorescence probe on the macroCTA initially starts in the aqueous phase but transfers to a hydrophobic environment after the conversion of THFA exceeds 11%.

In eq 2, log P_{oct} is a free energy term.[58] As such, molecules with positive log P_{oct} values spontaneously transfer from the water phase to the hydrophobic phase. This suggests that by 10 min, the environment surrounding the macroCTA is sufficiently hydrophobic to sequester the THFA monomer into monomer aggregates as we have hypothesized above. We therefore suggest that this is the cause of the initial large jump in lifetime. Over the next 20 min, the lifetime decreases as these monomer units are converted from an aggregated form into the growing polymer chain. Beyond 30−40 min, the ordered morphology forms and lifetime concomitantly begins to increase again, this time with morphology rather than hydrophobicity.

$$\log P_{oct} = -\frac{\Delta G_{transfer}}{RT \ln 10} \quad (2)$$

Fluorescence Lifetime Imaging Microscopy. Our final aim was to determine the suitability of this PISA system for the characterization of cellular behavior using FLIM. We first established whether the results discussed above from the TCSPC laser attachment on the fluorimeter would correlate with the 405 nm pulsed diode laser attachment on the confocal microscope. For this, 0.1 wt % solutions of each morphology were sandwiched between glass slides and directly imaged using FLIM (Figure 5A). All obtained images were analyzed using the fast-FLIM method for lifetime decay spectra and histograms (Figure 5B,C). It is important to note that at this point, as the nanoparticles were intended for cellular uptake, we chose to analyze a medium-length worm sample rather than the long worms as described above and excluded the poorly defined vesicles. This is because long aspect ratio cylindrical particles and highly dispersed particles have difficulties crossing

https://doi.org/10.1021/acs.macromol.3c01451
Macromolecules 2023, 56, 9443−9454

cell membranes, and therefore, we sought to prioritize morphologies with a higher chance of internalization.[59,60]

While the changes in lifetime were subtler compared to that of the solution state, an increase in lifetime decay values could clearly be observed as morphology evolved into higher-order structures. This was accompanied by observable changes in the lifetime histogram. For the macroCTA, the lifetime decay was rapid and showed a narrow distribution in the histogram (Figure 5C), whereas the small and large spheres showed a broader peak with a low maximum value and tailing toward longer lifetimes. The short and medium worms had peaks significantly shifted to the right indicating a longer overall lifetime, a negligible presence of shorter lifetime events, and some tailing toward longer lifetimes. The vesicles showed the broadest histogram, with a maximum quite close to the worm morphologies, but with a larger proportion of shorter and longer lifetime events. Direct lifetime tail fittings of the entire field of view are presented in Table S6. As with the solution-state measurements, the nanoparticles consistently showed a significantly larger contribution to the overall decay from longer-lived fluorophore states, which increased with higher-order morphology in comparison to that of the macroCTA alone. A visual comparison of these data shows quite clear qualitative differences in fluorophore behavior, even without formal emission fitting. This property enables ready analysis of fluorophore state to the nonexpert user, which facilitates the translation of this process into a wide range of pharmaceutical or industrial applications.

Finally, as a proof-of-concept, we demonstrated the potential of this maleimide PISA system as a cell imaging agent by studying the range of nanoparticle morphologies in a cellular environment. A549 lung cancer fibroblasts were chosen as the model cellular environment, and each nanoparticle morphology was first tested to confirm cytocompatibility at concentrations up to 0.1 wt % for 48 h (Figures S35 and S36). A549 cells were then incubated with small spheres, short worms, medium worms, and vesicles for 30 min, after which internalization was evaluated using confocal microscopy followed by FLIM to gain quantitative photophysical values within the cellular environment (Figure 5D). Confocal microscopy confirmed that all particle morphologies could be internalized within the cell cytosol, showing a diffuse pattern indicative of nonspecific uptake.[61] Of note, when solely analyzing the fluorescence images, all nanoparticle morphologies display the same qualitative emission data. In comparison, the images acquired using FLIM show obvious qualitative differences, in agreement with the images taken on glass slides. Owing to the lower resolution of FLIM (512 × 512 pixels), there was insufficient resolution to detect minute changes in the fluorophore state upon nanoparticle degradation events; however, future work is focused on extending the lifetime of the maleimide through chemistry design in order to improve on this. What was apparent, however, was that each lifetime histogram showed a general trend of shifting to the left, indicating that a greater proportion of shorter lifetime events occurred (Figure 5E). This is perhaps due to nanoparticle processing within the cellular environment causing the disassembly of the morphologies into single polymer chains; however, further experimentation is required to understand this observation.

Overall, the above results demonstrate the potential of this system to assist with imaging different particles when the same fluorophore is present due to the ability of the FLIM experiment to differentiate between the different morphologies. Further to this, we have presented a very promising concentration-independent fluorescence reporter system to enable the quantitative microscopy analysis of drug delivery platforms. We envision this becoming a powerful tool for the analysis of nanoparticle states within complex biological environments, where the maleimide moiety can provide unambiguous tracking of particle uptake and degradation. More broadly, this work has demonstrated a highly accurate and sensitive technique for the study of PISA mechanisms, while importantly maintaining accessibility and simplicity for other researchers in the field.

CONCLUSIONS

Here, we present the design and synthesis of a modular polymer platform for studying polymerization-induced self-assembly by using steady-state fluorescence and lifetime measurements. By incorporating an ACM moiety within a RAFT CTA, we were able to demonstrate that the PISA process can be studied in detail using the photophysical properties of the reporter. Importantly, inclusion of the maleimide unit did not impact polymer self-assembly on account of its small size and enabled unique and unambiguous characterization of nanoparticle morphologies using a combination of emission and lifetime decay analysis. In addition, the analysis of deconvoluted lifetime decay components enabled us to study the mechanism of PISA in the preonset of the assembly time frame, yielding information about premicellar aggregates that form in the early stages when targeting higher-order morphologies such as worms and vesicles. We further analyzed the hydrophobicity of the growing macroCTA via computational log P_{oct}/SA values to support the experimental observations during the PISA process. The applicability of this maleimide system to biological applications was demonstrated through confocal microscopy and FLIM, where the unique lifetime behavior of each was distinguishable within a cellular environment. We believe that the strategy presented herein will pave the way for further investigations into the use of polymeric materials as cell imaging agents and, more generally, for mechanistic studies of PISA in an accessible way.

ASSOCIATED CONTENT

Supporting Information

The Supporting Information is available free of charge at https://pubs.acs.org/doi/10.1021/acs.macromol.3c01451.

Materials and instrumentation, experimental procedures, and supplementary characterization data (PDF)

AUTHOR INFORMATION

Corresponding Author

Rachel K. O'Reilly − *School of Chemistry, University of Birmingham, Edgbaston, Birmingham B15 2TT, U.K.;* orcid.org/0000-0002-1043-7172; Email: r.oreilly@bham.ac.uk

Authors

Amanda K. Pearce − *School of Chemistry, University of Birmingham, Edgbaston, Birmingham B15 2TT, U.K.;* Present Address: Department of Chemistry, Loughborough University, Loughborough, LE11 3TU, United Kingdom

https://doi.org/10.1021/acs.macromol.3c01451
Macromolecules 2023, 56, 9443−9454

Sam J. Parkinson − *School of Chemistry, University of Birmingham, Edgbaston, Birmingham B15 2TT, U.K.*
Irem Akar − *School of Chemistry, University of Birmingham, Edgbaston, Birmingham B15 2TT, U.K.*
Matthew J. Derry − *Aston Advanced Materials Research Centre, Aston University, Birmingham B4 7ET, U.K.;* orcid.org/0000-0001-5010-6725
Paul D. Topham − *Aston Advanced Materials Research Centre, Aston University, Birmingham B4 7ET, U.K.;* orcid.org/0000-0003-4152-6976
Robert T. Mathers − *Department of Chemistry, Pennsylvania State University, New Kensington, Pennsylvania 15068, United States*
Vasilios G. Stavros − *Department of Chemistry, University of Warwick, Coventry CV4 7AL, U.K.;* Present Address: School of Chemistry, University of Birmingham, Edgbaston, Birmingham, B15 2TT, U.K; orcid.org/0000-0002-6828-958X

Complete contact information is available at: https://pubs.acs.org/10.1021/acs.macromol.3c01451

Author Contributions

The manuscript was written through the contributions of all authors. All authors have given their approval to the final version of the manuscript.

Funding

The authors thank the University of Birmingham for funding.

Notes

The authors declare no competing financial interest.

■ ACKNOWLEDGMENTS

The authors are grateful to Dr. Y. Xie for helpful discussions. This work was carried out with the support of Diamond Light Source, instrument I22 (proposal sm28511), and we would like to specifically acknowledge the support received by Prof. Nick Terrill, Dr. Andy Smith, and Dr. Paul Wady during our experiment.

■ REFERENCES

(1) Bates, C. M.; Bates, F. S. 50th Anniversary Perspective: Block Polymers-Pure Potential. *Macromolecules* **2017**, *50* (1), 3−22.
(2) Zhao, Y.; Sakai, F.; Su, L.; Liu, Y.; Wei, K.; Chen, G.; Jiang, M. Progressive Macromolecular Self-Assembly: From Biomimetic Chemistry to Bio-Inspired Materials. *Adv. Mater.* **2013**, *25* (37), 5215−5256.
(3) Tritschler, U.; Pearce, S.; Gwyther, J.; Whittell, G. R.; Manners, I. 50th Anniversary Perspective: Functional Nanoparticles from the Solution Self-Assembly of Block Copolymers. *Macromolecules* **2017**, *50* (9), 3439−3463.
(4) Penfold, N. J. W.; Yeow, J.; Boyer, C.; Armes, S. P. Emerging Trends in Polymerization-Induced Self-Assembly. *ACS Macro Lett.* **2019**, *8* (8), 1029−1054.
(5) Canning, S. L.; Smith, G. N.; Armes, S. P. A Critical Appraisal of RAFT-Mediated Polymerization-Induced Self-Assembly. *Macromolecules* **2016**, *49* (6), 1985−2001.
(6) Charleux, B.; Delaittre, G.; Rieger, J.; D'Agosto, F. Polymerization-Induced Self-Assembly: From Soluble Macromolecules to Block Copolymer Nano-Objects in One Step. *Macromolecules* **2012**, *45* (17), 6753−6765.
(7) Li, Y.; Armes, S. P. RAFT Synthesis of Sterically Stabilized Methacrylic Nanolatexes and Vesicles by Aqueous Dispersion Polymerization. *Angew. Chem., Int. Ed.* **2010**, *49* (24), 4042−4046.
(8) Hayward, R. C.; Pochan, D. J. Tailored Assemblies of Block Copolymers in Solution: It Is All about the Process. *Macromolecules* **2010**, *43* (8), 3577−3584.
(9) Grzelczak, M.; Vermant, J.; Furst, E. M.; Liz-Marzán, L. M. Directed Self-Assembly of Nanoparticles. *ACS Nano* **2010**, *4* (7), 3591−3605.
(10) Brotherton, E. E.; Hatton, F. L.; Cockram, A. A.; Derry, M. J.; Czajka, A.; Cornel, E. J.; Topham, P. D.; Mykhaylyk, O. O.; Armes, S. P. In Situ Small-Angle X-Ray Scattering Studies during Reversible Addition-Fragmentation Chain Transfer Aqueous Emulsion Polymerization. *J. Am. Chem. Soc.* **2019**, *141* (34), 13664−13675.
(11) Derry, M. J.; Fielding, L. A.; Warren, N. J.; Mable, C. J.; Smith, A. J.; Mykhaylyk, O. O.; Armes, S. P. In Situ Small-Angle X-Ray Scattering Studies of Sterically-Stabilized Diblock Copolymer Nanoparticles Formed during Polymerization-Induced Self-Assembly in Non-Polar Media. *Chem. Sci.* **2016**, *7* (8), 5078−5090.
(12) Fu, Y.; Finney, N. S. Small-Molecule Fluorescent Probes and Their Design. *RSC Adv.* **2018**, *8* (51), 29051−29061.
(13) Wu, D.; Sedgwick, A. C.; Gunnlaugsson, T.; Akkaya, E. U.; Yoon, J.; James, T. D. Fluorescent Chemosensors: The Past, Present and Future. *Chem. Soc. Rev.* **2017**, *46* (23), 7105−7123.
(14) Iliopoulos-Tsoutsouvas, C.; Kulkarni, R. N.; Makriyannis, A.; Nikas, S. P. Fluorescent Probes for G-Protein-Coupled Receptor Drug Discovery. *Expert Opin. Drug Discovery* **2018**, *13* (10), 933−947.
(15) Lee, M. H.; Kim, J. S.; Sessler, J. L. Small Molecule-Based Ratiometric Fluorescence Probes for Cations, Anions, and Biomolecules. *Chem. Soc. Rev.* **2015**, *44* (13), 4185−4191.
(16) Klymchenko, A. S. Solvatochromic and Fluorogenic Dyes as Environment-Sensitive Probes: Design and Biological Applications. *Acc. Chem. Res.* **2017**, *50* (2), 366−375.
(17) de Silva, A. P.; Gunaratne, H. Q. N.; Gunnlaugsson, T.; Huxley, A. J. M.; McCoy, C. P.; Rademacher, J. T.; Rice, T. E. Signaling Recognition Events with Fluorescent Sensors and Switches. *Chem. Rev.* **1997**, *97* (5), 1515−1566.
(18) Baghoth, S. A.; Sharma, S. K.; Amy, G. L. Tracking Natural Organic Matter (NOM) in a Drinking Water Treatment Plant Using Fluorescence Excitation-Emission Matrices and PARAFAC. *Water Res.* **2011**, *45* (2), 797−809.
(19) Bridgeman, J.; Bieroza, M.; Baker, A. The Application of Fluorescence Spectroscopy to Organic Matter Characterisation in Drinking Water Treatment. *Rev. Environ. Sci. Biotechnol.* **2011**, *10* (3), 277−290.
(20) Xu, W.; Zeng, Z.; Jiang, J. H.; Chang, Y. T.; Yuan, L. Discerning the Chemistry in Individual Organelles with Small-Molecule Fluorescent Probes. *Angew. Chem., Int. Ed.* **2016**, *55* (44), 13658−13699.
(21) Chan, J.; Dodani, S. C.; Chang, C. J. Reaction-Based Small-Molecule Fluorescent Probes for Chemoselective Bioimaging. *Nat. Chem.* **2012**, *4* (12), 973−984.
(22) Yuan, L.; Lin, W.; Zheng, K.; Zhu, S. FRET-Based Small-Molecule Fluorescent Probes: Rational Design and Bioimaging Applications. *Acc. Chem. Res.* **2013**, *46* (7), 1462−1473.
(23) Gao, P.; Pan, W.; Li, N.; Tang, B. Fluorescent Probes for Organelle-Targeted Bioactive Species Imaging. *Chem. Sci.* **2019**, *10* (24), 6035−6071.
(24) Lott, G. A.; Perdomo-Ortiz, A.; Utterback, J. K.; Widom, J. R.; Aspuru-Guzik, A.; Marcus, A. H. Conformation of Self-Assembled Porphyrin Dimers in Liposome Vesicles by Phase-Modulation 2D Fluorescence Spectroscopy. *Proc. Natl. Acad. Sci. U.S.A.* **2011**, *108* (40), 16521−16526.
(25) Yoo, H.; Yang, J.; Nakamura, Y.; Aratani, N.; Osuka, A.; Kim, D. Fluorescence Dynamics of Directly Meso-Meso Linked Porphyrin Rings Probed by Single Molecule Spectroscopy. *J. Am. Chem. Soc.* **2009**, *131* (4), 1488−1494.
(26) Mañas-Torres, M. C.; Gila-Vilchez, C.; González-Vera, J. A.; Conejero-Lara, F.; Blanco, V.; Cuerva, J. M.; Lopez-Lopez, M. T.; Orte, A.; Álvarez de Cienfuegos, L. In Situ Real-Time Monitoring of the Mechanism of Self-Assembly of Short Peptide Supramolecular Polymers. *Mater. Chem. Front.* **2021**, *5* (14), 5452−5462.

(27) Wang, Y.; Goodson, T. Early Aggregation in Prion Peptide Nanostructures Investigated by Nonlinear and Ultrafast Time-Resolved Fluorescence Spectroscopy. *J. Phys. Chem. B* **2007**, *111* (2), 327−330.
(28) Lu, S.; Wang, S.; Zhao, J.; Sun, J.; Yang, X. A PH-Controlled Bidirectionally Pure DNA Hydrogel: Reversible Self-Assembly and Fluorescence Monitoring. *Chem. Commun.* **2018**, *54* (36), 4621−4624.
(29) Wang, W.; Liu, J.; Li, C.; Zhang, J.; Liu, J.; Dong, A.; Kong, D. Real-Time and Non-Invasive Fluorescence Tracking of in Vivo Degradation of the Thermosensitive PEGlyated Polyester Hydrogel. *J. Mater. Chem. B* **2014**, *2* (26), 4185−4192.
(30) Huang, C. B.; Xu, L.; Zhu, J. L.; Wang, Y. X.; Sun, B.; Li, X.; Yang, H. B. Real-Time Monitoring the Dynamics of Coordination-Driven Self-Assembly by Fluorescence-Resonance Energy Transfer. *J. Am. Chem. Soc.* **2017**, *139* (28), 9459−9462.
(31) Garcia, A.; Blum, S. A. Polymer Molecular Weight Determination via Fluorescence Lifetime. *J. Am. Chem. Soc.* **2022**, *144* (49), 22416−22420.
(32) Wysocki, L. M.; Lavis, L. D. Advances in the Chemistry of Small Molecule Fluorescent Probes. *Curr. Opin. Chem. Biol.* **2011**, *15* (6), 752−759.
(33) Loudet, A.; Burgess, K. BODIPY Dyes and Their Derivatives: Syntheses and Spectroscopic Properties. *Chem. Rev.* **2007**, *107* (11), 4891−4932.
(34) Luo, S.; Zhang, E.; Su, Y.; Cheng, T.; Shi, C. A Review of NIR Dyes in Cancer Targeting and Imaging. *Biomaterials* **2011**, *32* (29), 7127−7138.
(35) Xie, Y.; Husband, J. T.; Torrent-Sucarrat, M.; Yang, H.; Liu, W.; O'Reilly, R. K. Rational Design of Substituted Maleimide Dyes with Tunable Fluorescence and Solvafluorochromism. *Chem. Commun.* **2018**, *54* (27), 3339−3342.
(36) Zhu, Q.; Ye, Z.; Yang, W.; Cai, X.; Tang, B. Z. One-Pot Synthesis and Structure-Property Relationship of Aminomaleimides: Fluorescence Efficiencies in Monomers and Aggregates Easily Tuned by Switch of Aryl and Alkyl. *J. Org. Chem.* **2017**, *82* (2), 1096−1104.
(37) Yeh, H. C.; Wu, W. C.; Chen, C. T. The Colourful Fluorescence from Readily-Synthesised 3,4-Diaryl-Substituted Maleimide Fluorophores. *Chem. Commun.* **2003**, *3* (3), 404−405.
(38) Kizaki, K.; Imoto, H.; Kato, T.; Naka, K. Facile Construction of N-Alkyl Arylaminomaleimide Derivatives as Intensively Emissive Aggregation Induced Emission Dyes. *Tetrahedron* **2015**, *71* (4), 643−647.
(39) Imoto, H.; Nohmi, K.; Kizaki, K.; Watase, S.; Matsukawa, K.; Yamamoto, S.; Mitsuishi, M.; Naka, K. Effect of Alkyl Groups on Emission Properties of Aggregation Induced Emission Active N-Alkyl Arylaminomaleimide Dyes. *RSC Adv.* **2015**, *5* (114), 94344−94350.
(40) Zheng, R.; Mei, X.; Lin, Z.; Zhao, Y.; Yao, H.; Lv, W.; Ling, Q. Strong CIE Activity, Multi-Stimuli-Responsive Fluorescence and Data Storage Application of New Diphenyl Maleimide Derivatives. *J. Mater. Chem. C* **2015**, *3* (39), 10242−10248.
(41) Xie, H. D.; Ho, L. A.; Truelove, M. S.; Corry, B.; Stewart, S. G. Fluorescent Triphenyl Substituted Maleimide Derivatives: Synthesis, Spectroscopy and Quantum Chemical Calculations. *J. Fluoresc.* **2010**, *20* (5), 1077−1085.
(42) Mabire, A. B.; Robin, M. P.; Quan, W. D.; Willcock, H.; Stavros, V. G.; O'Reilly, R. K. Aminomaleimide Fluorophores: A Simple Functional Group with Bright, Solvent Dependent Emission. *Chem. Commun.* **2015**, *51* (47), 9733−9736.
(43) Staniforth, M.; Quan, W. D.; Karsili, T. N. V.; Baker, L. A.; O'Reilly, R. K.; Stavros, V. G. First Step toward a Universal Fluorescent Probe: Unravelling the Photodynamics of an Amino-Maleimide Fluorophore. *J. Phys. Chem. A* **2017**, *121* (34), 6357−6365.
(44) Robin, M. P.; Mabire, A. B.; Damborsky, J. C.; Thom, E. S.; Winzer-Serhan, U. H.; Raymond, J. E.; O'Reilly, R. K. New Functional Handle for Use as a Self-Reporting Contrast and Delivery Agent in Nanomedicine. *J. Am. Chem. Soc.* **2013**, *135* (25), 9518−9524.
(45) Suhling, K.; Hirvonen, L. M.; Levitt, J. A.; Chung, P. H.; Tregidgo, C.; Le Marois, A.; Rusakov, D. A.; Zheng, K.; Ameer-Beg, S.; Poland, S.; Coelho, S.; Henderson, R.; Krstajic, N. Fluorescence Lifetime Imaging (FLIM): Basic Concepts and Some Recent Developments. *Med. Photonics* **2015**, *27*, 3−40.
(46) Sarder, P.; Maji, D.; Achilefu, S. Molecular Probes for Fluorescence Lifetime Imaging. *Bioconjug. Chem.* **2015**, *26* (6), 963−974.
(47) Rho, J. Y.; Scheutz, G. M.; Häkkinen, S.; Garrison, J. B.; Song, Q.; Yang, J.; Richardson, R.; Perrier, S.; Sumerlin, B. S. In Situ Monitoring of PISA Morphologies. *Polym. Chem.* **2021**, *12* (27), 3947−3952.
(48) Blanazs, A.; Madsen, J.; Battaglia, G.; Ryan, A. J.; Armes, S. P. Mechanistic Insights for Block Copolymer Morphologies: How Do Worms Form Vesicles? *J. Am. Chem. Soc.* **2011**, *133* (41), 16581−16587.
(49) Foster, J. C.; Varlas, S.; Couturaud, B.; Jones, J. R.; Keogh, R.; Mathers, R. T.; O'Reilly, R. K. Predicting Monomers for Use in Polymerization-Induced Self-Assembly. *Angew. Chem., Int. Ed.* **2018**, *57* (48), 15733−15737.
(50) Smith, A. J.; Alcock, S. G.; Davidson, L. S.; Emmins, J. H.; Hiller Bardsley, J. C.; Holloway, P.; Malfois, M.; Marshall, A. R.; Pizzey, C. L.; Rogers, S. E.; Shebanova, O.; Snow, T.; Sutter, J. P.; Williams, E. P.; Terrill, N. J. I22: SAXS/WAXS Beamline at Diamond Light Source-an Overview of 10 Years Operation. *J. Synchrotron Radiat.* **2021**, *28* (3), 939−947.
(51) Glatter, O.; Kratky, O.; Kratky, H. C. *Small Angle X-Ray Scattering*; Academic Press, 1982.
(52) Pervez, M.; Pearce, A. K.; Husband, J. T.; Male, L.; Torrent-Sucarrat, M.; O'Reilly, R. K. Enhancing Dual-State Emission in Maleimide Fluorophores through Fluorocarbon Functionalisation. *Chem.—Eur J.* **2022**, *28* (58), No. e202201877.
(53) Magenau, A. J. D.; Richards, J. A.; Pasquinelli, M. A.; Savin, D. A.; Mathers, R. T. Systematic Insights from Medicinal Chemistry To Discern the Nature of Polymer Hydrophobicity. *Macromolecules* **2015**, *48* (19), 7230−7236.
(54) Yildirim, E.; Dakshinamoorthy, D.; Peretic, M. J.; Pasquinelli, M. A.; Mathers, R. T. Synthetic Design of Polyester Electrolytes Guided by Hydrophobicity Calculations. *Macromolecules* **2016**, *49* (20), 7868−7876.
(55) Foster, J. C.; Akar, I.; Grocott, M. C.; Pearce, A. K.; Mathers, R. T.; O'Reilly, R. K. 100th Anniversary of Macromolecular Science Viewpoint: The Role of Hydrophobicity in Polymer Phenomena. *ACS Macro Lett.* **2020**, *9* (11), 1700−1707.
(56) Akar, I.; Foster, J. C.; Leng, X.; Pearce, A. K.; Mathers, R. T.; O'Reilly, R. K. Log Poct/SA Predicts the Thermoresponsive Behavior of P(DMA-Co-RA) Statistical Copolymers. *ACS Macro Lett.* **2022**, *11* (4), 498−503.
(57) Akar, I.; Keogh, R.; Blackman, L. D.; Foster, J. C.; Mathers, R. T.; O'Reilly, R. K. Grafting Density Governs the Thermoresponsive Behavior of P(OEGMA-Co-RMA) Statistical Copolymers. *ACS Macro Lett.* **2020**, *9* (8), 1149−1154.
(58) Bannan, C. C.; Calabró, G.; Kyu, D. Y.; Mobley, D. L. Calculating Partition Coefficients of Small Molecules in Octanol/Water and Cyclohexane/Water. *J. Chem. Theory Comput.* **2016**, *12* (8), 4015−4024.
(59) Hinde, E.; Thammasiraphop, K.; Duong, H. T. T.; Yeow, J.; Karagoz, B.; Boyer, C.; Gooding, J. J.; Gaus, K. Pair Correlation Microscopy Reveals the Role of Nanoparticle Shape in Intracellular Transport and Site of Drug Release. *Nat. Nanotechnol.* **2017**, *12* (1), 81−89.
(60) Zhao, W.; Ta, H. T.; Zhang, C.; Whittaker, A. K. Polymerization-Induced Self-Assembly (PISA) - Control over the Morphology of 19F-Containing Polymeric Nano-Objects for Cell Uptake and Tracking. *Biomacromolecules* **2017**, *18* (4), 1145−1156.
(61) Lee, J.; Sharei, A.; Sim, W. Y.; Adamo, A.; Langer, R.; Jensen, K. F.; Bawendi, M. G. Nonendocytic Delivery of Functional Engineered Nanoparticles into the Cytoplasm of Live Cells Using a Novel, High-

https://doi.org/10.1021/acs.macromol.3c01451
Macromolecules 2023, 56, 9443−9454

Throughput Microfluidic Device. *Nano Lett.* **2012**, *12* (12), 6322−6327.

https://doi.org/10.1021/acs.macromol.3c01451
Macromolecules 2023, 56, 9443−9454